

## Characteristics of cometary dust tracks in Stardust aerogel and laboratory calibrations

M. J. BURCHELL<sup>1\*</sup>, S. A. J. FAIREY<sup>1</sup>, P. WOZNAKIEWICZ<sup>2</sup>, D. E. BROWNLEE<sup>3</sup>, F. HÖRZ<sup>4</sup>, A. T. KEARSLEY<sup>2</sup>,  
T. H. SEE<sup>5</sup>, P. TSOU<sup>6</sup>, A. WESTPHAL<sup>7</sup>, S. F. GREEN<sup>8</sup>, J. M. TRIGO-RODRÍGUEZ<sup>9</sup>, and G. DOMÍNGUEZ<sup>10</sup>

<sup>1</sup>Centre for Astrophysics and Planetary Sciences, University of Kent, Canterbury, Kent CT2 7NH, UK

<sup>2</sup>Department of Mineralogy, The Natural History Museum, London SW7 5BD, UK

<sup>3</sup>Department of Astronomy, University of Washington, Seattle, Washington 98195, USA

<sup>4</sup>ARES, NASA Johnson Space Center, Houston, Texas 77058, USA

<sup>5</sup>ESCG, NASA Johnson Space Center, Houston, Texas 77058, USA

<sup>6</sup>Jet Propulsion Laboratory, California Institute of Technology, Pasadena, California 91109–8099, USA

<sup>7</sup>Department of Physics, University of California at Berkeley, Berkeley, California 94720

<sup>8</sup>Planetary and Space Science Research Institute, Open University, Milton Keynes MK7 6AA, UK

<sup>9</sup>Institute of Space Sciences (CSIC), Campus UAB, Facultat de Ciències, Torr C-5, parells, 2a planta, 08913 Bellaterra, Spain and Institut d'Estudis Espacials de Catalunya (IEEC), Ed. Nexus, Gran Capita, 2-4, 08034 Barcelona, Spain

<sup>10</sup>Department of Chemistry and Biochemistry, University of California San Diego, La Jolla, California 92093–0356, USA

\*Corresponding author. E-mail: M.J.Burchell@kent.ac.uk

(Received 11 December 2006; revision accepted 21 July 2007)

**Abstract**—The cometary tray of the NASA Stardust spacecraft's aerogel collector was examined to study the dust captured during the 2004 flyby of comet 81P/Wild 2. An optical scan of the entire collector surface revealed 256 impact features in the aerogel (width >100 µm). Twenty aerogel blocks (out of a total of 132) were removed from the collector tray for a higher resolution optical scan and 186 tracks were observed (track length >50 µm and width >8 µm). The impact features were classified into three types based on their morphology. Laboratory calibrations were conducted that reproduced all three types. This work suggests that the cometary dust consisted of some cohesive, relatively strong particles as well as particles with a more friable or low cohesion matrix containing smaller strong grains. The calibrations also permitted a particle size distribution to be estimated for the cometary dust. We estimate that approximately 1200 particles bigger than 1 µm struck the aerogel. The cumulative size distribution of the captured particles was obtained and compared with observations made by active dust detectors during the encounter. At large sizes (>20 µm) all measures of the dust are compatible, but at micrometer scales and smaller discrepancies exist between the various measurement systems that may reflect structure in the dust flux (streams, clusters etc.) along with some possible instrument effects.

## INTRODUCTION

The use of silica aerogel (originally developed as a low-density material by Kistler [1931], with ultra-low densities available in recent decades), as an ultra-low-density transparent solid to capture relatively intact samples of projectiles impacting at speeds in excess of a few km s<sup>−1</sup> was demonstrated in the laboratory (Tsou et al. 1988); a recent review of subsequent developments is given by Burchell et al. (2006). In brief, silica aerogel is a solid foam, essentially a dried SiO<sub>2</sub> gel with an open network of pores. The low densities obtainable today for aerogel (which range from just

over 1 to approximately 500 kg m<sup>−3</sup>), are the consequence of this pore space inside an otherwise solid material. Projectiles travelling at hypervelocity speed (of the order of km s<sup>−1</sup>) normally undergo severe damage on impact with a solid (nonporous) target of density much greater than aerogel. Typically during such impacts, the front of the projectile slows but is then crushed by the rear of the projectile (which has not yet slowed) and the target material cannot initially move away from the impact point to respond to the impact, thus generating a shock wave. The result is that extremely high densities and shock pressures are generated in both the projectile and target materials. During adiabatic release from

Table 1. Properties of glass beads used in calibration work. Impact speeds are accurate to better than 1%.

Nominal diameter $\pm\sigma$ ( $\mu\text{m}$ )	Measured diameter $\pm\sigma$ ( $\mu\text{m}$ ) <sup>a</sup>	Impact speed ( $\text{km s}^{-1}$ )
$11.58 \pm 0.19$	$9.8 \pm 2.2$	6.07
$35.0 \pm 0.8$	$34.7 \pm 1.0$	5.99
$63.8 \pm 0.8$	$64.1 \pm 2.8$	5.82

<sup>a</sup>See Kearsley et al. (2006).

this shocked state (which can involve pressures of tens or even hundreds of GPa), heating of the materials occurs. Most of the projectile is then vaporized, and only a few percent of it can be subsequently found at the impact site, usually in the form of a melt lining part of the crater that forms in the target.

In aerogel, however, the impact process is different and is more of a “penetration” event than a cratering one. The peak pressures generated on collision with such a low-density medium are insufficient to melt typical silicate-impactors, sometimes even insufficient to cause projectile fragmentation. Such projectiles tunnel into the aerogel, losing speed as a continual process (see Anderson and Ahrens [1994] for a general model for capture of hypervelocity particles in mesoporous foams and Domínguez et al. [2004] for a recent model of capture specific to aerogel). At some  $6 \text{ km s}^{-1}$ , the projectile may penetrate a factor of 100–200 deeper into aerogel compared to crater depth in solids such as rock or metal, producing a long, readily visible penetration track with a captured and typically unmelted particle at the end. During capture, there is some heating of the aerogel that can melt and form a molten wrap around the particle; some of the projectile surface is heated and shed as an ablative process. Depending on the nature of the impactor, a relatively intact particle can be found at the end of a track in the aerogel afterward. How much of the particle is captured depends on impact speed, aerogel density, and projectile structure and composition, but at  $5\text{--}6 \text{ km s}^{-1}$ , as much as 60, 70, or even 100% of relatively competent particles some tens of micrometers across can be captured (see Burchell et al. 2006). Alternatively, the impact process can so severely disrupt the particle that it effectively breaks apart into a large number of fragments lining the wall of a wide cavity in the aerogel. And some inhomogeneous particles give a combination of these two capture possibilities, resulting in tracks that are a mixture of the large, broad cavity plus discrete subsidiary tracks emerging from it. This is discussed in more detail later.

Given that silica aerogel is highly transparent, and that the particle fragments (large or small) are easily observable and readily extractable for detailed characterization with state-of-the-art analytical instruments, aerogel became the collector medium of choice for retrieving cosmic dust, i.e., dust in space that is travelling at speeds of  $\text{km s}^{-1}$  relative to the observer. Several space missions have deployed aerogel dust collectors in low-Earth orbit (reviewed in Burchell et al. 2006).

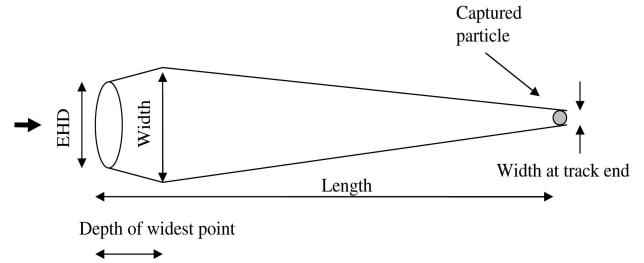


Fig. 1. Schematic of typical carrot-shaped track observed in laboratory impacts of glass beads in aerogel. Key dimensions are labeled. EHD = entrance hole diameter. Note that the width at track end is not always the same as the mean diameter of the captured particle. Impact direction was from left.

The NASA Stardust mission to comet 81P/Wild 2 deployed an aerogel dust collector (Brownlee et al. 2003) as it flew past the comet at 1.86 AU from the Sun, with a relative encounter speed of  $6.1 \text{ km s}^{-1}$  (Brownlee et al. 2004; Tsou et al. 2004). At this heliocentric distance, the comet was actively ejecting dust and gas. The speed of the dust grains (with respect to the comet) was low compared to the fly-by speed of the spacecraft so the impact on the aerogel was at a constant encounter speed of  $6.1 \text{ km s}^{-1}$  and normal incidence. The Dust Flux Monitor Instrument (DFMI), an active impact sensor on the spacecraft’s leading edge, indicated that during the encounter dust grains were indeed striking the spacecraft, and it predicted a flux for the entire aerogel collector of  $2800 \pm 500$  cometary grains larger than  $15 \mu\text{m}$  in diameter (Tuzzolino et al. 2004), although an impact ionization detector (sensitive to smaller particles) indicated a much lower flux (Kissel et al. 2004).

The successful return of the Stardust aerogel collector to Earth in January 2006 provided access to the cometary material captured in the aerogel. The first reports (Brownlee et al. 2006; Hörz et al. 2006; and other papers in the same issue of *Science*) have already provided a wealth of detail from the preliminary examination (PE) post-flight analysis effort. In this paper, we provide an in-depth analysis of the characteristics of the tracks observed in the Stardust cometary aerogel, combined with a description of experimental impacts that simulated the Stardust environment, thus providing insights and “calibrations” for the Stardust observations.

## LABORATORY CALIBRATION

### Laboratory Impacts with Glass Beads

The calibration of track size as a function of impactor size or mass is greatly aided by the fact that the encounter speed of Stardust was a constant  $6.1 \text{ km s}^{-1}$  at normal incidence to the collector surface. The experiments employed the same soda-lime glass beads that were used to calibrate the crater size in Stardust aluminum foils (Kearsley et al. 2006). These glass beads were supplied by Whitehouse Scientific Ltd.; their

Table 2. Average track dimensions measured in the aerogel.

Nominal diameter $\pm\sigma$ ( $\mu\text{m}$ )	Number of tracks	Track length ( $\mu\text{m}$ )	Entrance hole diameter ( $\mu\text{m}$ )	Maximum width ( $\mu\text{m}$ )	Depth of maximum width ( $\mu\text{m}$ )	Captured particle diameter ( $\mu\text{m}$ )	Track volume ( $\text{mm}^3$ )
$11.58 \pm 0.19$	6	$2131 \pm 529$	$84 \pm 35$	$114 \pm 33$	$238 \pm 130$	$15 \pm 2$	$0.010 \pm 0.007$
$35.0 \pm 0.8$	5	$9309 \pm 1755$	$178 \pm 22$	$467 \pm 73$	$2026 \pm 769$	$34.8 \pm 1.8$	$0.643 \pm 0.235$
$63.8 \pm 0.8$	5	$17,598 \pm 837$	$379 \pm 76$	$750 \pm 144$	$1108 \pm 331$	$66.0 \pm 2.4$	$3.10 \pm 1.32$

characteristics are given in Table 1. In Kearsley et al. (2006), particle sizes were measured independently of the supplier's nominal values and good agreement was found. Using the University of Kent two-stage light-gas gun (Burchell et al. 1999a), samples beads in three size ranges were fired into Stardust-grade aerogel manufactured as part of the same batches used in the Stardust cometary aerogel collector. This aerogel did not have a uniform density; instead it varied across the 3 cm thickness of the blocks, from  $5 \text{ kg m}^{-3}$  at the front face to  $50 \text{ kg m}^{-3}$  at the rear face (Tsou et al. 2003). The impact speeds were measured for each shot to better than 1% and are given in Table 1. Tracks were observed with the classic carrot shape, i.e., the entrance hole widening quickly to a maximum track width just below the surface and then tapering with (nonparallel) straight-line sides to a near point where the particle was captured (see schematic in Fig. 1). Note that the maximum track width is not at the entrance hole, but occurs at some small depth below it.

For each size of projectile, several tracks were measured under the microscope. The various parameters measured are defined as follows: track length is the straight line distance from center of the entrance hole in the surface plane of the aerogel to the center of the captured particle. The entrance hole diameter is the average of several measurements; the holes are not necessarily circular, so two orthogonal diameters are taken and averaged; any narrow fractures in the surface plane that emanate from the main hole are ignored. The maximum track width is measured transverse to the main track axis (i.e., track length) at its widest point and the depth of this position below the original aerogel surface is also recorded. The captured particle may not be spherical; accordingly, two orthogonal diameters are taken and averaged. The average values for the measurements of each quantity are given in Table 2. The uncertainty given on each average value is the  $1\sigma$  value of the distribution in each case. On average, the maximum track width occurred 13% of the total track length below the entrance hole (although there is a large scatter on this). The data for track length (L), entrance hole diameter (EHD) and greatest width (W) are plotted versus original particle diameter (OPD) in Fig. 2 (various fits are shown and are described as follows). In Fig. 2a, it is found that:

$$L = -(1287 \pm 669) + (296 \pm 19) \times \text{OPD} \quad (1)$$

where units are in  $\mu\text{m}$ . This can be re-arranged to obtain:

$$\text{OPD} = [L + (1287 \pm 669)] / (296 \pm 19) \quad (2)$$

where all units are  $\mu\text{m}$ . If the fit is forced to pass through the

origin, then we obtain  $L = (271 \pm 10) \times \text{OPD}$  (dashed line in the figure), which is very similar to the original fit.

The data for EHDs are shown in Fig. 2b, along with three fits. The first fit is a linear fit, which gives:

$$\text{EHD} = (14 \pm 46) + (5.0 \pm 1.4) \times \text{OPD} \quad (3)$$

Again units are  $\mu\text{m}$  and the results can be rearranged as:

$$\text{OPD} = [\text{EHD} - (14 \pm 46)] / (5.0 \pm 1.4) \quad (4)$$

If the linear fit is constrained to pass through the origin, we obtain  $\text{EHD} = (5.3 \pm 0.6) \times \text{OPD}$ , shown as a dashed line in the figure and very similar to the original linear fit. The third fit considered in Fig. 2b is a polynomial fit. As can be seen in the figure, although in the size range used it tracks the data points themselves, this fit does not approach the origin at small values of OPD, a nonphysical result for small-sized particles. This is typical of fits to any of the calibration data, where a linear fit is always found to describe the data well. With this caveat about failing for small particles, the fit yields:

$$\text{EHD} = (60 \pm 71) + 1.38 \times \text{OPD} + 0.057 \times \text{OPD}^2 \quad (5)$$

(units are  $\mu\text{m}$ ). This can be solved as a quadratic to give the original particle diameter for a particular value of entrance hole diameter (EHD).

$$\text{OPD} = \{-1.38 \pm \sqrt{[1.904 - 0.228 \times (60 - \text{EHD})]}\} / 0.114 \quad (6)$$

In Fig. 2c, the greatest track width data are shown and are again fitted twice. Both fits are linear. The first (solid line) only uses the three data points and gives:

$$W = -(36 \pm 50) + (13.3 \pm 2.3) \times \text{OPD} \quad (7)$$

units are in  $\mu\text{m}$ . Rearranging gives:

$$\text{OPD} = [(36 \pm 50) + W] / (13.3 \pm 2.3) \quad (8)$$

The intercept on this fit is a finite value but is within  $1\sigma$  of zero. Accordingly, we refit (dashed line), requiring the linear fit to pass through the origin, and obtain:

$$W = (12.1 \pm 0.5) \times \text{OPD} \quad (9)$$

which rearranged yields:

$$\text{OPD} = W / (12.1 \pm 0.5) \quad (10)$$

where units are  $\mu\text{m}$ .

As well as the directly measured quantities, it was also possible to estimate the volume of each track. This was done by approximating the track shape as a series of congruent frustra. A frustum is a symmetrical truncated cone, as shown in Fig. 3a.

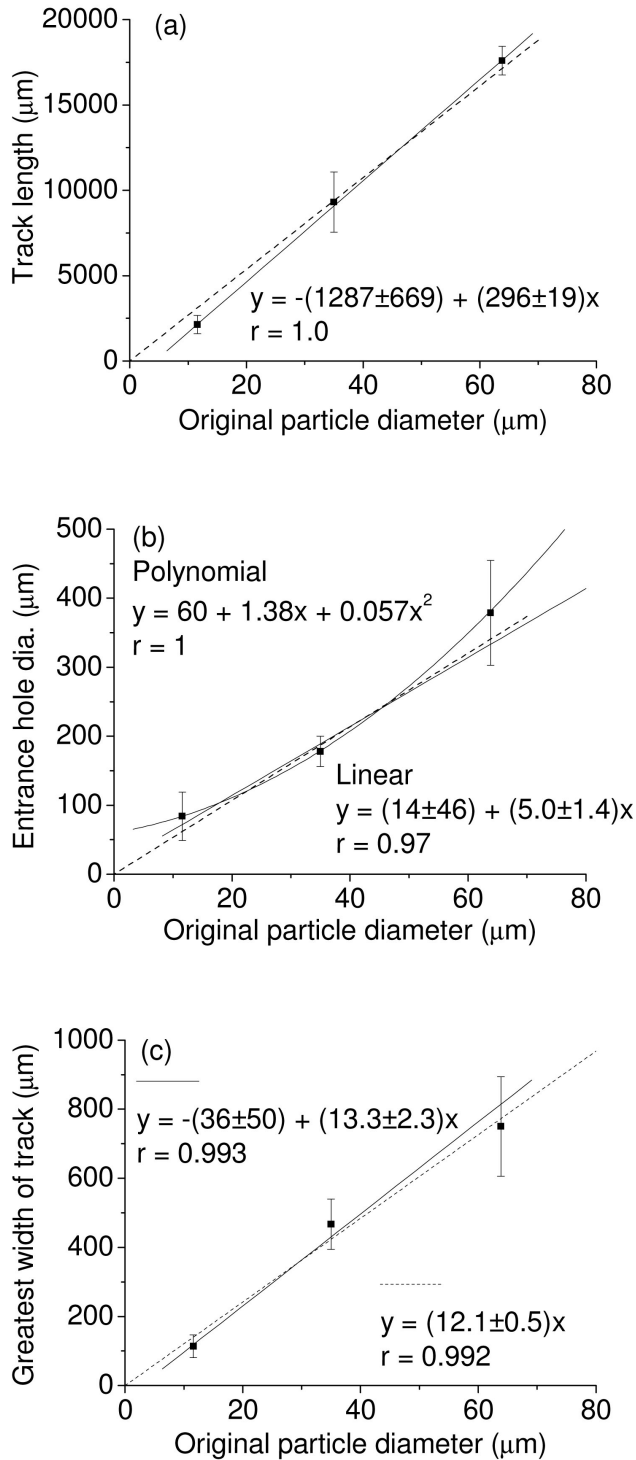


Fig. 2. Calibration shots in aerogel. a) Average track length versus original particle diameter. b) Average entrance hole diameter versus original particle diameter. c) Average greatest track width versus original particle diameter. Parameterizations of the fit curves are given in the figure (and explained in the main text as Equations 1, 3, 5, and 7) along with  $r$ , the regression coefficient of the fit.

Two such shapes can be combined to approximate a carrot track shape (Fig. 3b). The key measurements of a frustum were all available from the track measurements. These were then used to obtain the volume ( $V$ ) of the three-dimensional track. On selected tracks, volume measurements were made by slicing the track into 20 or 40 individual cells and finding the volume of each. Agreement in the results with the two-frustum method was at the level of 10–15%, indicating reasonable robustness in the method. The average results for volume are given in Table 2 and plotted versus impact kinetic energy (KE) in Fig. 4. The KEs were obtained for each sample using the nominal particle size and the mean mass combined with the speed of each shot. This yields energies of  $3.5 \times 10^{-5}$  J,  $9.1 \times 10^{-4}$  J and  $6.02 \times 10^{-3}$  J, respectively, for the 11.58, 35, and 63.8 μm diameter samples. The fit to Fig. 4 gives:

$$V = -(0.011 \pm 0.009) + (600 \pm 170) \times \text{KE} \quad (11)$$

where units are  $\text{mm}^3$  for volume and J for KE. Rearranging this gives:

$$\text{KE} = \{V + (0.011 \pm 0.009)\} / (600 \pm 170) \quad (12)$$

where again units are  $\text{mm}^3$  for volume and J for KE. This suggests 1.7 mJ of energy are needed to excavate each cubic mm of aerogel, with an accuracy of about 28%. That the intercept is only just over  $1\sigma$  away from zero, suggests this relation also holds for smaller tracks than those measured here.

In general, there is a degree of surprise about these results. For example, it has previously been shown (e.g., Hörz et al. 1998; Burchell et al. 2006) that for impacts at equal speed by similarly sized particles, track length increases as aerogel density decreases. Here, impacts of different sized projectiles into density gradient aerogel have produced a simple dependence of, for example, track length on particle size. Detailed modelling is underway to evaluate the origin of these dependences and to determine the actual density gradient in the top 10 mm of Stardust aerogel tiles. It should also be noted that with only three data points in each calibration data set here, although linear fits are shown to be good descriptions of the data, any fine non-linear dependencies are not discernible rather than completely excluded.

Using these results, it is possible to measure track length, entrance hole diameter, or greatest track width and obtain an estimate of the diameter of the original impacting particle on the Stardust collector. In the case of track volume the calibration gives an impact energy (based on the volume of aerogel excavated). For the known impact speed of Stardust, a particle mass can then be found. If a density is assumed the particle diameter can then be obtained.

The above relationships were obtained for soda-lime glass beads (density  $2.4 \text{ g cm}^{-3}$ ) impacting the aerogel. Whether these can then be directly applied to other types of particles requires consideration. In the case of entrance hole diameters, it is reasonable to assume that the critical parameter is particle diameter. For example, Burchell et al.

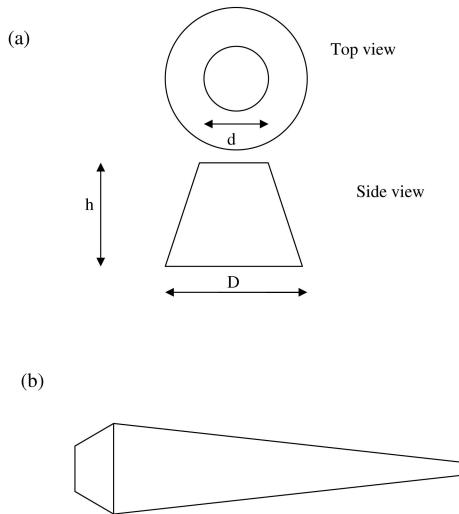


Fig. 3. a) Top and side views of a frustum shape. b) Side view of two frustums, which approximate the carrot track shape shown in Fig. 1.

(1999b) have shown that particles of olivine, soda glass, and iron 100 microns in diameter all leave similarly sized entrance holes in aerogel. This seems reasonable if we consider the analogy as penetration of a very thin sheet; at hypervelocities the hole punched in thin films gives a good measure of particle cross-sectional area (Hörz et al. 1994). If taken further, this analogy may suggest that similarly to the thin film, the continuous aerogel medium does not exhibit a major flow field around the surface entrance hole. Track length should not, however, be taken as a good indicator of particle size, as this may well depend on additional properties of the particle (e.g., density, which will affect impact energy or melting point that will affect the mass loss during penetration). Greatest track width is also not an ideal parameter, although it is accurate for tracks similar in shape to those obtained in the calibration; in the Stardust aerogel other track morphologies are also seen. Track volume may be a good indicator of impact kinetic energy, as the data suggest a constant excavation energy per  $\text{mm}^3$  of aerogel for the soda-lime glass impactors used in the present experiments. This assumes no extra source of energy (i.e., from chemical decomposition of the projectile during capture). This will be returned to later when applied to real data from Stardust.

### Laboratory Impacts with a Variety of Minerals and Basalt

As well as glass beads, impacts on Stardust cometary grade aerogels were obtained in the laboratory with four types of natural materials. These were to simulate impacts from a typical range of materials possibly representative of those likely to be found at a comet. Details of the materials are given in Table 3. The olivine and basalt grains produced carrot tracks in the aerogel similar to Fig. 1, these are called type A. The

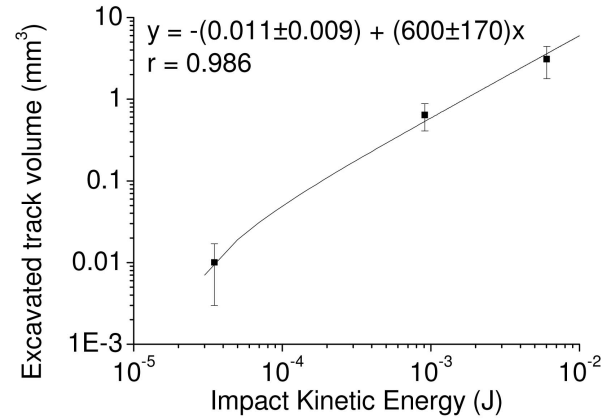


Fig. 4. The estimated average track volume versus impact kinetic energy is shown for the calibration shots in aerogel. The parameterization of the fit curve (Equation 11; see main text) is given on the figure along with  $r$ , the regression coefficient of the fit.

pyrrhotite grains produced type B tracks, i.e., tracks with a slightly broader initial cavity which then tapered down to a carrot track. This has the appearance of a champagne flute wine glass without the base (i.e., only a bowl and a stem region). This is shown in Fig. 5a. The lizardite grains, however, produced type C tracks with a broad cavity and no individual tracks emerging from it (Fig. 5b); the walls of these cavities were lined with fine fragments of particles, some of which had penetrated slightly into the aerogel beyond the edge of the cavity. Several such broad cavity tracks were seen in the aerogel from the lizardite impacts. A typical cavity is shown at centimeter-size scale in Fig. 5b; we also observed similar impact features at millimeter-scale. This behavior is thus not size-dependent. However, in the lizardite shot, there were also some impacts that gave type B tracks with discrete fragments (of lizardite) at the end of the stylus. The size distribution of these trapped grains (and the associated large scatter in track length) did not reflect the size of the initial particles, suggesting they may have broken up during launch before impacting the aerogel.

There are thus three types of tracks observed in these shots and the morphological classification used is that which was also used in Hörz et al. 2006. Type A (soda-lime glass, basalt, olivine) is the classic carrot-shaped aerogel track, which initially broadens to a maximum width below the initial impact point, then has (nonparallel) near-straight lined walls that come to a point (with the trapped particle nearby). Type B (pyrrhotite and some lizardite) are also relatively slender tracks, but have a broader initial cavity than the glass projectiles and curved walls, which taper to a thinner stem from which emerges a carrot-shaped track, terminating near a captured particle. Type C tracks (some lizardite particles) have only a broad cavity and no stem emerging from it, with no large discrete fragments of the initial particle beneath the cavity; instead multiple small fragments line the cavity.

Table 3. Mineral and basalt shots into Stardust-grade aerogel in the laboratory. Impact speeds are accurate to better than 1%.

Projectile	Source	Impact speed ( $\text{km s}^{-1}$ )	Grain size ( $\mu\text{m}$ ) <sup>a</sup>
Basalt	Natural History Museum (London). USGS sample NKT-1G	6.09	1–several hundred $\mu\text{m}$
Pyrrhotite	Natural History Museum (London) BM.2005.M317	5.85	<125
Lizardite	Natural History Museum (London). Confirmed by X-ray diffraction.	5.94	>53
Olivine	LLNL, San Carlos olivine	5.85	<45

<sup>a</sup>This was at launch; some minerals may break apart into a smaller size range during the shock of launch.

There has been previous experimental work which has produced aerogel tracks of various shapes. Hörz et al. (1998) observed impacts in aerogel (density  $20 \text{ kg m}^{-3}$ ) in the laboratory at speeds up to  $6 \text{ km s}^{-1}$ . As well as carrot-shaped tracks from glass beads, they also observed types B and C tracks from impacts of compressed dry cocoa powder (made from micron-sized grains). Type B tracks were obtained by mixing aluminum or glass spheres ( $50 \mu\text{m}$ ) with the cocoa powder, and type C tracks by pure cocoa powder projectiles. When examined afterward, the cocoa powder was found to line the wall of the cavities. Their conclusion was that low-cohesion projectiles leave bulbous, type C cavities, but cohesive projectiles produce carrot-shaped type A tracks. Mixtures of the two types of material inside one inhomogeneous particle would produce a track type that was a cross between these two extremes, i.e., a type B track. There is thus good agreement with the types of tracks found in the mineral shots here in Stardust grade aerogels and the work of Hörz et al. (1998). One difference is that the bulbous cavities in the lizardite shots here may arise from a high volatile content of the projectile (lizardite is typically 14% water by mass) whereas in Hörz et al. (1998), it was due to low cohesive strength of a fine-grained matrix. At potentially higher, albeit unknown, impact speeds, Hörz et al. (2000) also observed similar track morphologies in aerogel exposed on the Mir Space Station. Separately, Kitazawa et al. (1999) proposed a scheme for track categorization. For impacts at  $>4 \text{ km s}^{-1}$ , they found three track types (similar to those here) from impacts into aerogel of density  $30 \text{ kg m}^{-3}$ . There is thus good agreement between three separate sets of experiments indicating that three major types of tracks are obtained from impacts in aerogel. In the remainder of this work, we use the names types A, B, or C to label each type. The transition between types (and variation inside types) is totally gradational.

Although three types of tracks are found, the entrance holes appear similar (a typical entrance hole is shown in Fig. 6). Thus the entrance hole does not differentiate between track type. Although the mineral grains were not monodisperse,



Fig. 5. Tracks made by impact of: (a) pyrrhotite grains in aerogel at  $5.85 \text{ km s}^{-1}$ ; the largest track just extends off the bottom of the image so the captured grain is not visible. b) Lizardite grain in aerogel at  $5.94 \text{ km s}^{-1}$ ; the incident grain has broken up/disaggregated into many fine fragments which are too small to be visible at this scale but line the walls of the cavity in the aerogel. In both cases the impact direction was from the top.

the range of entrance hole sizes in each shot is compatible with that expected from the known particle size range and the calibration for soda-lime glass (Fig. 2b; Equations 3 and 5). This indicates that entrance hole diameter is probably the most suitable parameter to use for determining particle size from impacts in aerogel of unknown particles. However, due to the highly transparent nature of aerogel and some intrinsic surface roughness, it can be difficult to focus on the surface face of an aerogel block and obtain a well-resolved image of an entrance hole, especially at small track sizes.

## STARDUST COMETARY TRAY TRACKS

### Level 2 Scan

The returned Stardust aerogel samples were examined in a dedicated Class 100 clean room at the NASA Curatorial Facilities in Houston, Texas. The cometary aerogel tray contained 132 cells of aerogel, 130 of which were rectangular with slightly rounded corners (surface of nearly  $4 \text{ cm} \times 2 \text{ cm}$ ), but two were trapezoid-shaped, with a width of  $2 \text{ cm}$  and

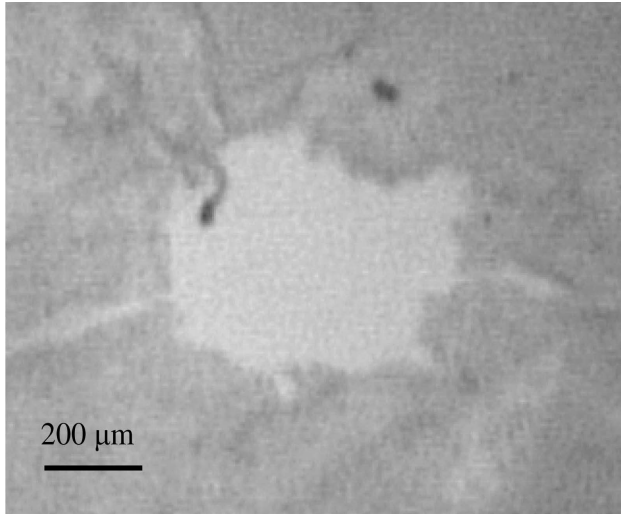


Fig. 6. Top view of the entrance hole in aerogel made by the impact of a soda-lime glass bead ( $63.8 \mu\text{m}$  in diameter) at  $5.82 \text{ km s}^{-1}$  in the laboratory.

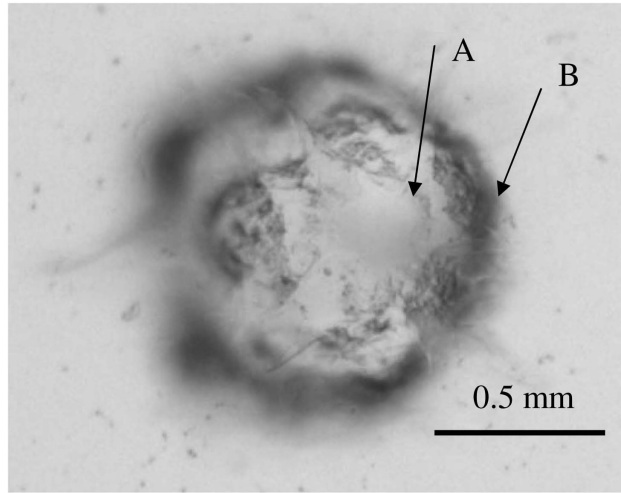


Fig. 8. Example entrance holes in Stardust cometary aerogel (track CO27-T4). The edge of the hole in the top surface is shown indicated by arrow A. The edge of the region of widest extent in the subsurface is also shown indicated by arrow B.

lengths of 3 and 2 cm on the long sides. The total surface area of aerogel was  $1039 \text{ cm}^2$ . All cells were 3 cm deep. The aerogel density was not less than  $5 \text{ kg m}^{-3}$  at the front surface, increasing to no more than  $50 \text{ kg m}^{-3}$  at the rear. Full details are in Tsou et al. (2003). The aerogel blocks were held in an aluminum frame with an appearance like a tennis racket (see Fig. 7), with each cell held in place by soft aluminum foil along the walls of the cell and over the sides of the supporting frame. The blocks could be removed by cutting these foils on the flat top of the frame and pulling the foil from the rear to slide the block out. The exposed surfaces of these foils were also analyzed for impact features (Hörz et al. 2006; Kearsley et al. 2007).

Prior to any sample processing, all cometary aerogel

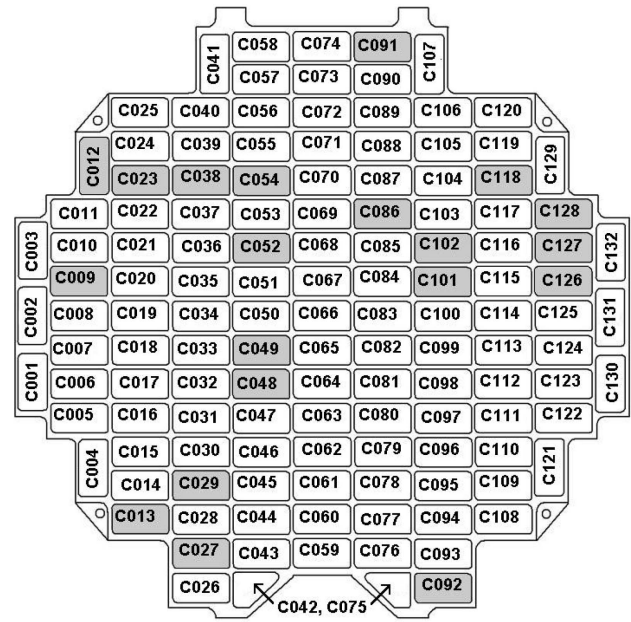


Fig. 7. Layout of aerogel blocks in cometary aerogel collector tray. Each block is labeled with its Stardust designator Cnnn, where “nnn” is an integer in the range 1–132.

surfaces were imaged, via optical microscope/CCD at  $16\times$  (and in some cases also at  $20\times$ ) magnification, typically producing some 42 images for each individual aerogel block at a resolution of approximately  $3.5$  (or  $2.7$ , respectively)  $\mu\text{m}/\text{pixel}$ . This is referred to as Level 2 Stardust photography documentation. Because the aerogel cells still resided in the modular openings of the collector tray, this photography depicts all tracks in plan view (from above or at  $15^\circ$  inclination). Systematic analysis of these mosaics and of individual framelets was conducted for all 132 aerogel blocks, aided by the iterative microscopic inspection of actual tiles to clarify the nature of some features that seemed ambiguous in the images. An example entrance hole is shown in Fig. 8 (note that tracks are numbered in the style Cnnn-Tm, where nnn is the 3 digit number referring to the aerogel piece in the collector tray [see Fig. 7], and m is an integer 1, 2, 3... for the first, second, third, etc., track found in that block). Although the imagery was focused on a cell's surface, determination of the entry hole was difficult in most cases, as features at some depth in the transparent medium often interfered. Thus the parameter most readily measured in a systematic fashion in plan view is the maximum diameter (W) of individual tracks, modestly below the surface, yet still in reasonable focus. The threshold for reliable track recognition during this tray wide survey was empirically set at  $W = 100 \mu\text{m}$ , a compromise between actual resolution, surface roughness, and operator time. This survey produced a total of 256 tracks  $>100 \mu\text{m}$  diameter; Fig. 9 illustrates their size frequency. The accuracy of the measurements was  $\pm 10 \mu\text{m}$ , and accordingly at the smallest sizes the data are grouped in 10 micron bins. The greatest track width recorded was  $9.961 \text{ mm}$ . The distribution of these features across the surface of the aerogel

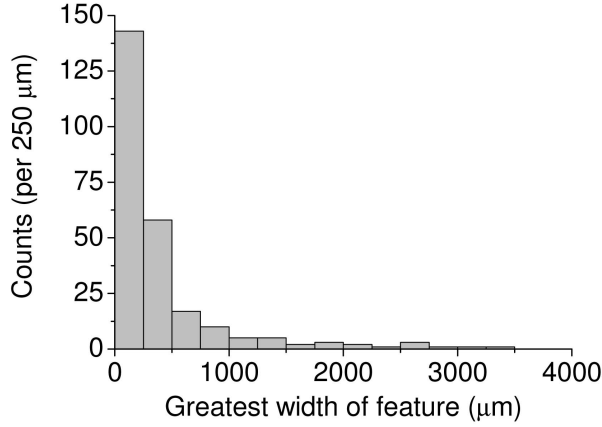


Fig. 9. Size frequency of features seen on Level 2 scan. In addition, there are four features greater than 4 mm in size.

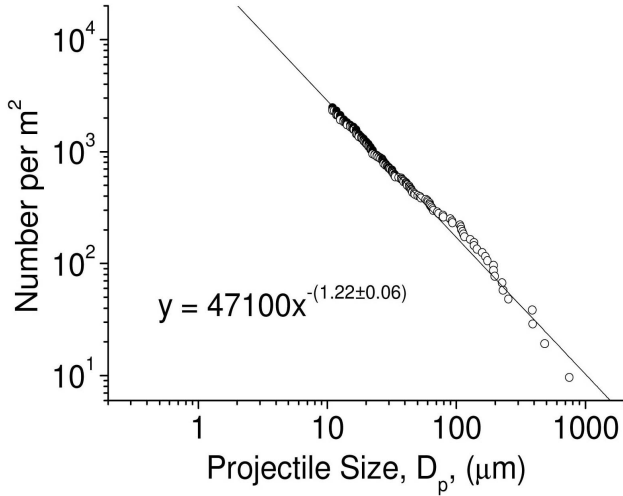


Fig. 11. Cumulative particle size distribution for the cometary aerogel collector based on an optical (Level 2) scan of the whole aerogel surface while it was still in the collector tray (before any individual aerogel cells were removed from analysis). The fit curve shown is described in the text (Equation 13).

collector is shown in Fig. 10. Given 132 aerogel blocks and 256 features, approximately two per block are expected for a random distribution.

To generate a preliminary impact flux for the whole cometary aerogel collector, a calibration has to be applied. The relation of Equation 8 is used to provide estimates of projectile diameter  $D_p$  (note that for greatest widths of diameter,  $>100 \mu\text{m}$ , there is little difference between use of Equations 8 or 10). The resulting cumulative particle size was given in Hörz et al. (2006) and is shown in Fig. 11. As expected, the distribution cuts off at about  $10 \mu\text{m}$  in  $D_p$  and extends up to almost 1 mm. Ignoring the largest few particles (where small statistics may cause fluctuations), a fit to the data from 10 to  $200 \mu\text{m}$  gives:

$$\text{Cumulative size distribution per m}^2 = 47100 D_p^{-1.22 \pm 0.06} \quad (13)$$

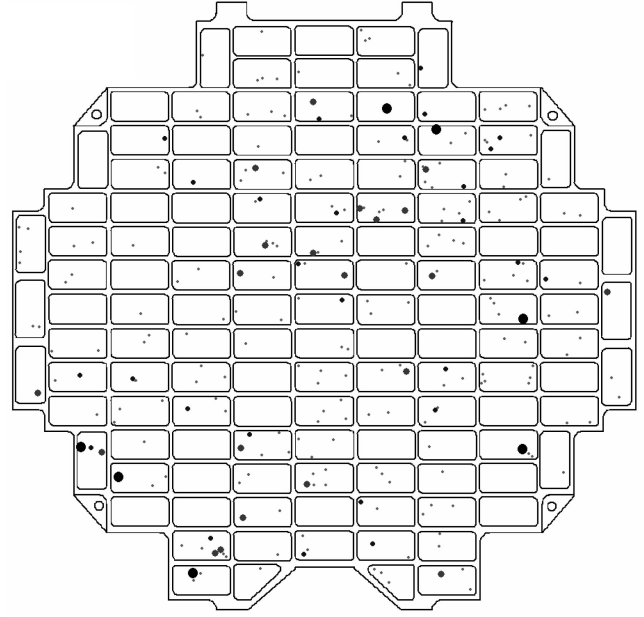


Fig. 10. Distribution of Level 2 features across the aerogel collector. Feature diameter is represented by symbol size: • is 100–500  $\mu\text{m}$ , • is 500–1000  $\mu\text{m}$ , • is 1000–5000  $\mu\text{m}$ , and • is 5000–10,000  $\mu\text{m}$ .

At larger sizes, the slope in the cumulative flux increases somewhat, but as stated, this may be due to the statistics of small numbers of events. The lack of a roll-off in the flux at smaller sizes indicates a fairly complete degree of scanning. Based on this flux, we find that 180 particles greater than  $15 \mu\text{m}$  in diameter struck the aerogel.

However, some caution is required in fully accepting this estimate of the flux. The calibration used was obtained from the experimental type A tracks. However, as will be seen below, the data here are a mixture of track types. As already stated, it is not certain if maximum track width for a given value of  $D_p$  is independent of track type. Type B tracks are wider than type A by perhaps a factor of 2 (based on rough estimates made from the calibration shots of lizardite). So a fraction of tracks in the cumulative flux in Fig. 11 may have had their  $D_p$  overestimated by a similar factor. Since type A tracks dominate at small track lengths, the true slope in Fig. 11 is probably slightly steeper than that in Equation 13.

### Level 3 Scan

After the whole tray survey, 20 cometary cells of aerogel were initially removed from the tray and their analysis is given here (shown as shaded blocks in Fig. 7 and listed in Table 4) (Note that additional cells have been removed subsequently either for analysis or long-term curatorial storage). The removed cells were then imaged side-on, where each tile was rotated some  $15^\circ$  to permit viewing of the exposed surface from below, which substantially improved



## Cometary aerogel trays used in this work

C009, C012, C013, C023, C027, C029, C038, C048, C049, C052, C054, C086, C091, C092, C101, C102, C118, C126, C127, C128

(compared to perfectly orthogonal views) the recognition of very small tracks. This so-called Level 3 Stardust photography documentation was conducted at magnifications of up to 16 $\times$ , 25 $\times$ , 32 $\times$ , 50 $\times$ , 63 $\times$ , or even 100 $\times$ , with a resolution of 3.4, 2.2, 1.7, 1.1, 0.88 or 0.55  $\mu\text{m}$  per pixel, respectively, modestly higher than Level 2. Also, each tile was photographed in discrete depth intervals, progressing in 2.5 mm steps from the front to the rear side, resulting in 8 “slices,” each slice consisting of some 64 images. The purpose of this photography was to produce a permanent record of the size and X/Y location of the track population in a given tile. Additionally, most of the large tracks were photographed individually, with an optimally adjusted focal plane. The extracted blocks represented some 15% of the total aerogel in the cometary tray, which was sufficient to provide a high-resolution survey of tracks in the collector. The rest of the tray is currently being preserved by NASA as a resource for future analysis.

A total of 206 possible track-like features were initially noted in the Level 3 images. One feature was excluded as it had impacted on the edge of the supporting aluminum frame and the resulting debris had spread into the aerogel; 19 features were discarded because they were somewhat ambiguous and not verified by a second observer. This gave a set of 186 tracks in the 20 aerogel blocks. Due to their small size and faint images, nine of these tracks could only have their dimensions measured to worse than 20% accuracy. The remaining 177 tracks were measured to higher accuracy, with the largest measured to better than 1%. The minimum track length was 55  $\mu\text{m}$  and the smallest maximum track width measured was 6  $\mu\text{m}$ .

The tracks were visually categorized into type using the 186 track data set. Examples are shown in Fig. 12 (type A), Fig. 13 (type B), and Fig. 14 (type C). In Fig. 12b, the captured particle at the end of a type A track is shown. In Fig. 13, very thin tracks can be seen emerging almost radially (with a slight downward tilt) from the main cavity. Fine grains of particulate material line the main cavity and are seen along these fiber-like tracks and the stylus, as well as there being a terminal particle at the end of the stylus. Many of these fragments are micron scale and suitable for analysis by a variety of techniques. Thus a single type B track may contain many identifiable particle fragments suitable for compositional studies. There is a very fine division between types B and C, several tracks listed as B are close to type C, possessing only very short styli emerging beneath the main cavity.

Averaged over all sizes, 65% of tracks were type A, 33% type B, and 2% type C. However, this was found to be size-dependent. A breakdown of the percentage of types A and B versus track length is given in Fig. 15 and given numerically

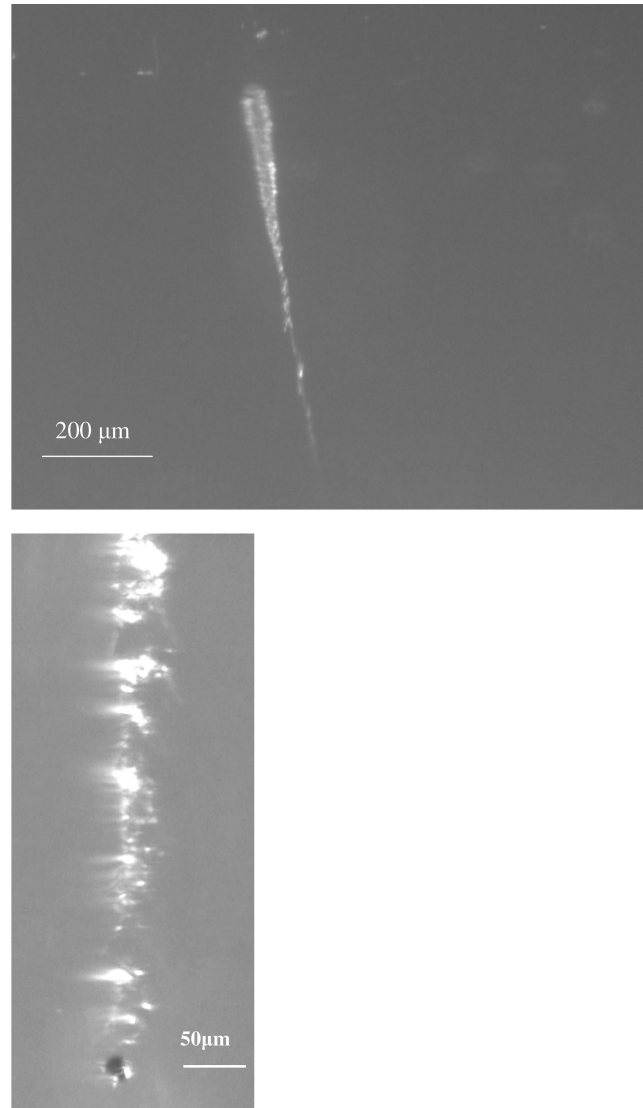


Fig. 12. Examples of type A impacts from Stardust cometary aerogel tray (Level 3 images). a) Typical track (C038-T7). b) Captured terminal particle (bottom) at end of track (from C086-T2). In both cases, the impact direction was from the top.

in Table 5. For small track lengths (<100  $\mu\text{m}$ ), all tracks are given as type A. There is a problem here as the resolution is starting to become comparable to track width, and although the tracks do not appear to have a transition region along their length (which would indicate a type B track if it were seen), higher resolution imaging is required to determine if this is indeed the case. For tracks greater than 500  $\mu\text{m}$  in length, 50% are A's and 50% B's. In the track length ranging from 100 to 500  $\mu\text{m}$ , there is a gradual transition from one regime to the other. At larger track lengths (>1500  $\mu\text{m}$ ), the small statistics prevent meaningful comparison. The four type C tracks were spread over all lengths in proportion to where the bulk of the tracks occurred, indicating no favored size scale.

In some impacts of type A, the incident particle appears

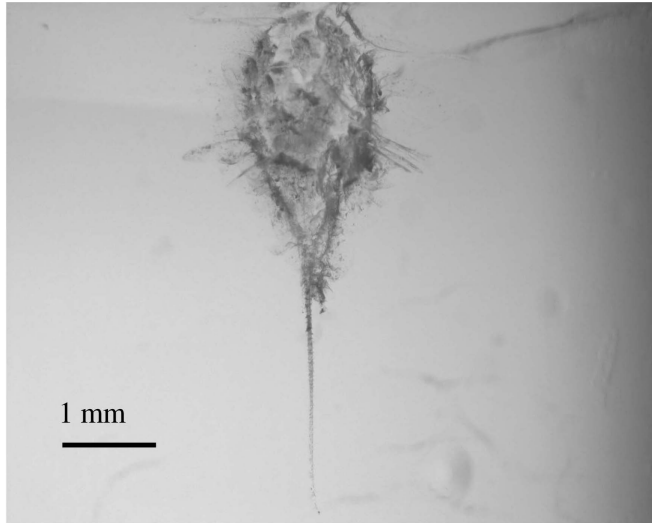


Fig. 13. Example of a type B impact (C054-T3) from the Stardust cometary aerogel tray (Level 3 images). Impact direction was from the top.

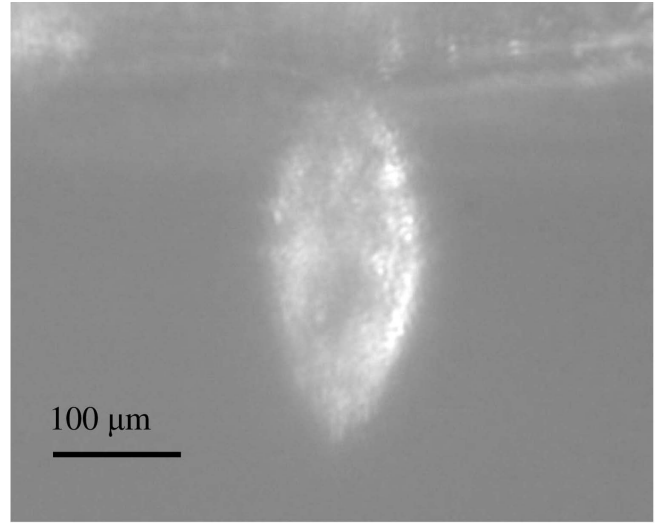


Fig. 14. Example of a type C track (C052-T6) from the Stardust cometary aerogel tray (Level 3 images). Impact direction was from the top.

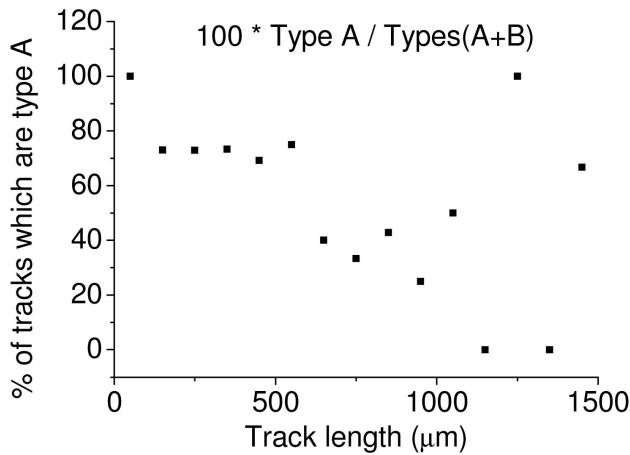


Fig. 15. The percent of tracks that are type A, defined as  $100 \times \Sigma A / \Sigma(A + B)$  versus track length (bin width 100  $\mu\text{m}$ ). For the longest tracks, the quantization of 0, 66, or 100% at long track lengths is due to small numbers of tracks per bin.

to have split during capture, and resulted in more than one terminal track (or “stylus”) per impact. This is also true for type B tracks, where several styli can be seen emerging beneath the main cavity (and are clearly distinct in size from the radial-hair-like features seen in Fig. 13). The distribution of how many styli are found in each track type is shown in Fig. 16. There is a clear difference between track types. Type A tracks are dominated by single terminal particles (86%). Type B tracks have one terminal particle just under 50% of the time, two in one-third of occurrences and 21% of type B tracks have three or more terminal particles. This suggests a different nature to the particles causing types A and B tracks. Type A particles are stronger materials, well-consolidated into usually a single grain. Type B particles are weaker in

some fashion, either more loosely bound or more volatile-rich, and are more readily disrupted into fragments during capture.

Each track was then individually measured. The key measurements were total track length ( $L$ ) from entrance hole to the deepest penetrating discrete fragment (or bottom of cavity for type C tracks), entrance hole diameter (EHD), and maximum track width ( $W$ ). In addition, for types B and C tracks, the main cavity was divided into several contiguous frustra and the necessary heights and widths obtained. For all tracks, if more than 1 stylus was observed, each was measured separately (and treated as being similar to a carrot-shaped track, i.e., it had a base diameter and length that served to define a cone shape for the stylus). From the set of measurements made for each track, an estimate of track volume ( $V$ ) was then obtained, treating each track as a set of frustums or cones as required (similar to the treatment of the calibration data).

The distribution of maximum track widths versus lengths is shown in Fig. 17. The track lengths ranged from 50 to 10,000  $\mu\text{m}$ . Track widths ranged from 4 to 2000  $\mu\text{m}$ . A strong correlation was observed between track width and length (indicated by the near-diagonal trend in the data in Fig. 17). The data displayed in Fig. 17 have been grouped by track type. A division between the types is possible (with a few exceptions close to the boundaries). The division between types A and B is given by:

$$W = 0.065 \times L^{1.1} \quad (14)$$

and between types B and C by:

$$W = 0.20 \times L^{1.1} \quad (15)$$

As noted above, at short track lengths ( $L < 100 \mu\text{m}$ ), only type A tracks are observed. It is possible that for the shortest tracks, the imaging resolution is insufficient to clearly

Table 5. Track categories versus track length (some percents do not sum to 100 due to rounding errors).

Track length range	% type A	% type B	% type C
All	65	33	2
<100 $\mu\text{m}$	100	0	0
100–500 $\mu\text{m}$	70	27	3
500–1000 $\mu\text{m}$	49	49	3
>1000 $\mu\text{m}$	51	49	0

distinguish between types A and B. The tracks appear at current resolution as “fat” cylinders with only some slight tapering toward their terminus. They are thus apparently not type B, but are, however, relatively broader than the type A track seen at larger scales. This assignment should thus be used cautiously and will be the subject of future work at higher resolutions.

The ratio  $W/L$  is informative for tracks, as it indicates how relatively thin or fat a track is.  $W/L$  is shown versus track length in Fig. 18. The lines shown in Fig. 18 divide the data into distinct regions. At low track lengths (<100  $\mu\text{m}$ , shown by a vertical solid line) only type A tracks are seen (as noted earlier). The main population of types A and B tracks are mostly separated by a horizontal line shown at  $W/L = 0.11$ , while the main population of type B and C tracks are separated by a horizontal line shown at  $W/L = 0.35$ . Ignoring the region  $L < 100 \mu\text{m}$ , track type A thus has  $W/L < 0.11$ , type B has  $0.11 \leq W/L < 0.35$ , and type C has  $W/L \geq 0.35$ . Some type B tracks do intrude into the region defined for type C. Renewed examination of these shows that the terminal track in these type B tracks is visible, but is typically very short and narrow (in some images similar short tracks are seen radiating near laterally from higher up the main cavity), indicating the presence of a very small fragment of the original particle.

In Fig. 19 the track volumes are shown versus track length for all tracks. Figure 19a shows type A tracks, and the data were fitted to yield:

$$V = 0.043 \times L^{(2.47 \pm 0.08)} \quad (16)$$

where  $L$  is in  $\mu\text{m}$  and  $V$  in  $\mu\text{m}^3$ . The behavior of the data for  $L < 100 \mu\text{m}$  seems to differ somewhat for that at larger track lengths. Accordingly, this data was excluded from the fit and a new relation obtained for type A tracks ( $L > 100 \mu\text{m}$ ) of:

$$V = 0.012 \times L^{(2.66 \pm 0.09)} \quad (17)$$

As might be expected, the power in Equation 17 has increased slightly compared to Equation 16. Both fits are shown on the plot (all data solid line,  $L > 100 \mu\text{m}$  as a dashed line). In Fig. 19b, the data are given for type B tracks and these yield a fit:

$$V = 0.0072 \times L^{(3.01 \pm 0.10)} \quad (18)$$

where again  $L$  is in  $\mu\text{m}$  and  $V$  in  $\mu\text{m}^3$ . In Fig. 19c, all data are shown combined into one plot. Ignoring the region for  $L < 100 \mu\text{m}$  (boundary marked by a vertical line), we find that the boundary between type A and B tracks is given by:

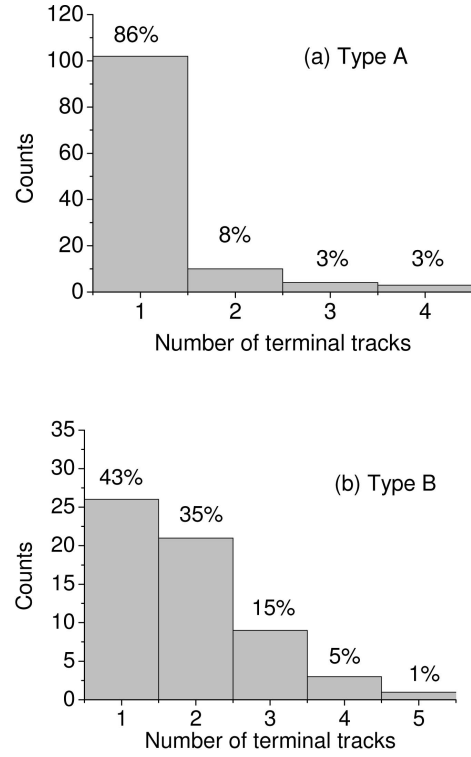


Fig. 16. Frequency of the number of terminal tracks (“styli”) for (a) type A tracks and (b) type B tracks.

$$V = 0.003 \times L^3 \quad (19)$$

and between types B and C by:

$$V = 0.05 \times L^3 \quad (20)$$

In most cases, attempts to directly measure the size of the captured particles from the Level 3 images failed as the particles were at or below the limits of resolving and measuring such tiny grains in the images. More detailed images of the captured particles were made for a few tracks as part of the compositional analysis studies, which are reported elsewhere in this volume.

The measured values for track volume were then combined with the calibration data (Equation 12) to obtain estimates of the pre-impact particle diameters in each track. The assumption made was that all particles had a density of  $2400 \text{ kg m}^{-3}$ . The results are shown versus track length in Fig. 20. The projectile sizes ranged from 0.4 to 100 micron. The cumulative size plot is shown in Fig. 22. At small sizes (<1  $\mu\text{m}$ ) the cumulative size distribution flattens off, indicating a loss in scanning efficiency rather than a lack of smaller particles. At large particle diameters, the data are susceptible to the statistics of small numbers and the cumulative curve shows a sudden change in slope. Finally, the total size distribution of Fig. 21 was fit over the range 1–100  $\mu\text{m}$ , yielding:

$$\text{Cumulative size distribution per m}^2 = 11900 D_p^{-0.76 \pm 0.01} \quad (21)$$

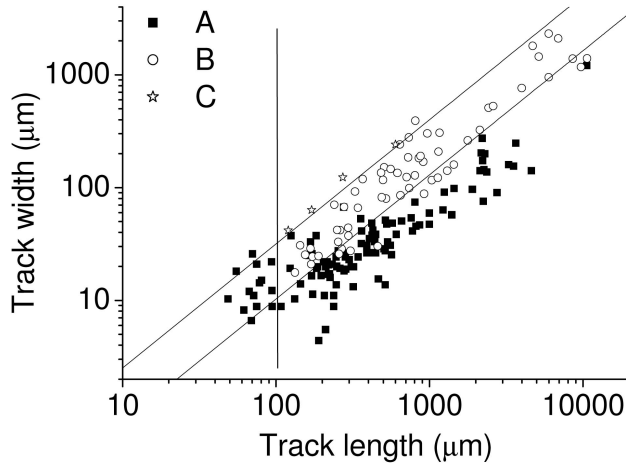


Fig. 17. Stardust cometary aerogel track widths versus lengths (Level 3 scan). Track types are as indicated. See main text for details of the boundary lines superimposed on the data.

From Equation 21, the number of particles bigger than  $1\text{ }\mu\text{m}$  in diameter striking the Stardust aerogel tray is predicted to be approximately 1200, and the number of particles larger than 15 micron diameter is predicted to be 158 particles. This latter value is compatible with that predicted by the Level 2 scan of the entire tray, which predicted 180 particles greater than  $15\text{ }\mu\text{m}$  in diameter. And as shown in Hörz et al. (2006), the size distribution (ignoring clustering, which is discussed in the next section and can lead to significant variations in flux on small surface areas) is compatible with the average size distribution obtained from the craters on the aluminum foils at that size scale. This is however, substantially less than the  $2800 \pm 500$  particles greater than  $15\text{ }\mu\text{m}$  predicted by the DFMI during the flyby in 2004 (Tuzzolino et al. 2004).

## DISCUSSION

### Calibration and Classification of Stardust Aerogel Tracks

The calibration is based on two data sets. The first concerns measured track parameters (length, volume, etc.) obtained from mono-dispersive glass beads fired into Stardust-grade aerogels in the laboratory. The second uses polydispersive grains of various materials, again fired at Stardust-grade aerogels in the laboratory. In both cases, the data sets are revealing and provide the necessary insights into capture in the Stardust aerogels. However, both could be further extended. The present limitation is operational and related to the lack of more Stardust-grade aerogel. This situation may be improved in the near future when the original Stardust aerogel manufacturing procedure may be repeated to provide more aerogel for calibration purposes. It will then be possible to conduct calibrations with mono-

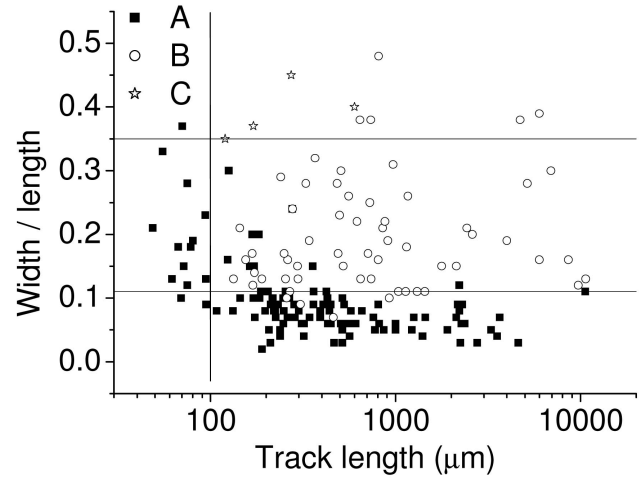


Fig. 18. Ratio of track width/length versus track length. Track types are as shown. See the text for details of the boundary lines superimposed on the data.

dispersive particles of a range of densities as has been done for the cratering in Stardust foils (Kearsley et al. 2007). Similarly, fine details of the capture mechanism and how it changes the nature of the impactor (e.g., processing of organics during capture) can be studied in more depth.

The data herein concerning tracks in the Stardust aerogel from the cometary collector side were obtained during the PE period up until August 2006. They thus represent a first look at the aerogel. Work is ongoing, and more data will be available later as more blocks are removed for analysis. However, the current data sets are large enough to show the main trends in the analysis, although in some cases (e.g., the type C tracks) there are still low statistics that, if improved, may reveal more. In general, it is unlikely that many more large tracks will be found. However, with greater statistics and particularly higher resolution images for the very short tracks, the track morphological classification can almost certainly be improved and the nature of the tracks at the smallest scales clarified further. One major point to note, however, is that the data refer only to the cometary collector tray. The interstellar collector tray still awaits an equivalent analysis when the first imaging of the tray is complete by the Stardust@home analysis effort.

One notable feature of the observed tracks is their distribution across the collector as observed in the Level 3 scan of extracted aerogel cells shown in Fig. 22. The observed number counts per cell are not compatible with a random distribution. This effect is strongly correlated with feature size (i.e., particle size). For larger particles, the distribution is nearly compatible with a random distribution, but for the smallest particles this is not the case. This is discussed in detail in a separate paper (Westphal et al. 2008).

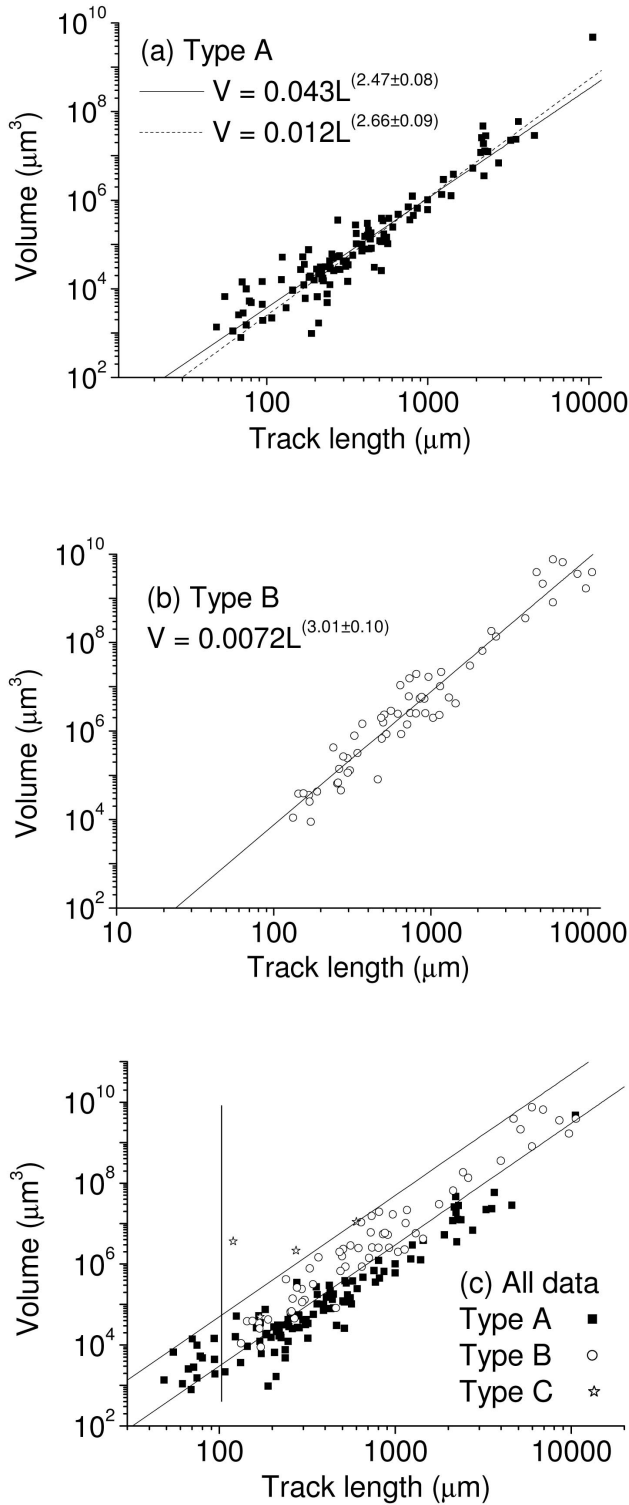


Fig. 19. Track volume ( $V$ ) versus track length ( $L$ ) for tracks measured in the Stardust cometary aerogel. a) Type A tracks. b) Type B. c) All data. The fit curves shown in (a) and (b) are Equations 16, 17, 18 as described in the text. The boundary lines shown in (c) are Equations 19 and 20 as described in the text.

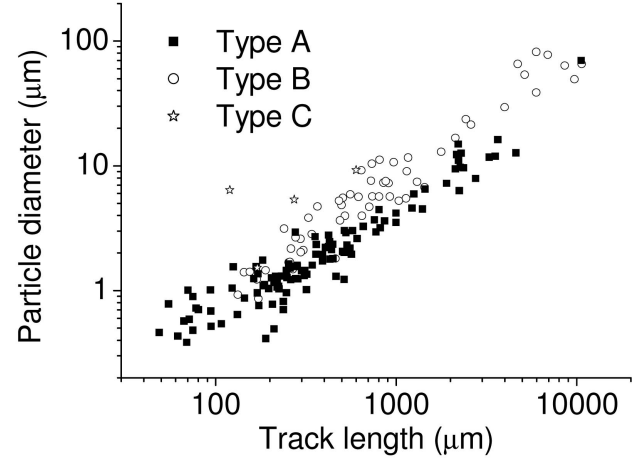


Fig. 20. Estimated particle size versus track length for tracks measured in the Stardust cometary aerogel. Particle size was obtained from Equation 12 in the text.

### Cumulative Size Distribution and Flux

The cumulative size distribution obtained from the data reported in depth in this paper can be compared to that obtained by analysis of the cratering in the aluminum foils in Stardust and the flux measured during the cometary encounter by electronic instruments read out in real time. All methods can yield a size distribution, but the active instruments (DFMI) also provide timing information reflecting on the spatial distribution of the dust near the comet. In the following discussion, all data have been converted to particle sizes assuming a density of  $2.4 \text{ g cm}^{-3}$ . While this may be a reasonable assumption for the density of individual grains, particles with high porosity may have a significantly lower bulk density.

In summary, there are two cumulative size distributions calculated from the features in the aerogel (see above and Table 6). The first is based on the Level 2 scan of surface features of the whole collector tray and the second is based on the higher resolution Level 3 scan of tracks (side view) in the aerogel blocks (15% of the total) removed during the PE period. The two thus use different data sets: the former is complete at large sizes (impactors nearly up to a millimeter in size) but loses sensitivity at intermediate sizes (10  $\mu\text{m}$  impactor size), while the latter is never complete per se, but is sensitive to smaller impact features, extending the impactor size range down to 0.5  $\mu\text{m}$ . The Level 2 and 3 data sets are shown on the same axes in Fig. 23. A fit to the combined Level 2 and 3 results was made over the size range 1 to 200  $\mu\text{m}$  in projectile size, and gave (dotted line on Fig. 23):

$$\text{Cumulative size distribution per m}^2 = 14100 D_p^{-0.86 \pm 0.01} \quad (22)$$

It can be seen in Fig. 23 that at small sizes the aerogel data rolls off and is probably incomplete due to

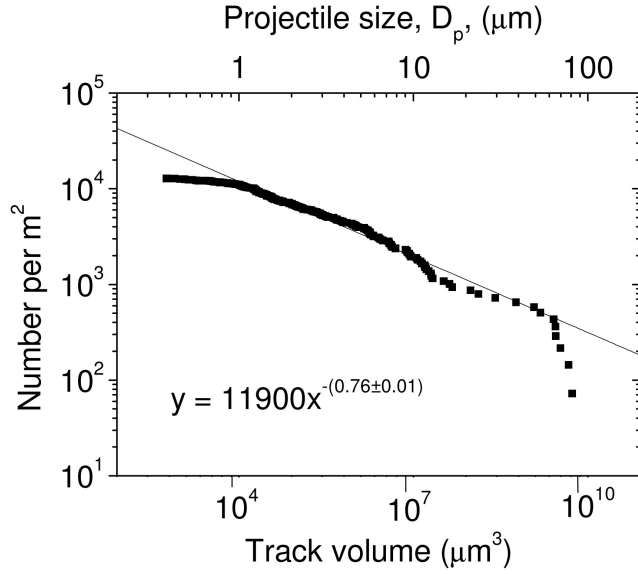


Fig. 21. Cumulative particle size distribution based on a high resolution optical (Level 3) scan of the 20 aerogel blocks extracted from the Stardust cometary dust collector tray. The fit curve shown is described (Equation 21) in the main text.

limited resolution. At large sizes, a single fit no longer describes all the data (with the data falling below the fit result).

These results can be compared to those previously reported by the Stardust PE team. In Hörz et al. (2006), Fig. 4 shows the cumulative size distribution data. The fit that was given in that paper was based on the craters measured in the aluminum foils carried by Stardust. Using the calibration in Kearsley et al. (2006), the crater widths (rim crest to rim crest) were converted to impactor diameter. This calibration used impacts of soda-lime glass beads onto Stardust-grade foils (similar in nature to those used here for the aerogel, with diameters in the size range 10–84  $\mu\text{m}$ ). Two sets of Stardust craters were used in obtaining the impactor size distribution. The first was called “large” craters ( $>10 \mu\text{m}$  in diameter) and represent the tray-wide sum of such craters on all foils, akin to the Level 2 track observations. The second category was small craters ( $<5 \mu\text{m}$  in diameter), which were obtained from higher resolution SEM scans of selected sub-areas of the foils that were harvested and allocated during PE. After application of the calibration (i.e., assuming the impactors were spheres of density  $2.4 \text{ g cm}^{-3}$ ), the small craters correspond to impactors sized 20 nm to  $1 \mu\text{m}$  (and thus are smaller than the projectiles used in the calibration) and the large craters to impactors sized 4 to  $100 \mu\text{m}$  (roughly covering the calibration projectile size range). A single fit to the combined crater data over the impactor size range 0.05 to  $100 \mu\text{m}$  yielded:

$$\text{Cumulative size distribution per m}^2 = 125800 D_p^{-1.72 \pm 0.05} \quad (23)$$

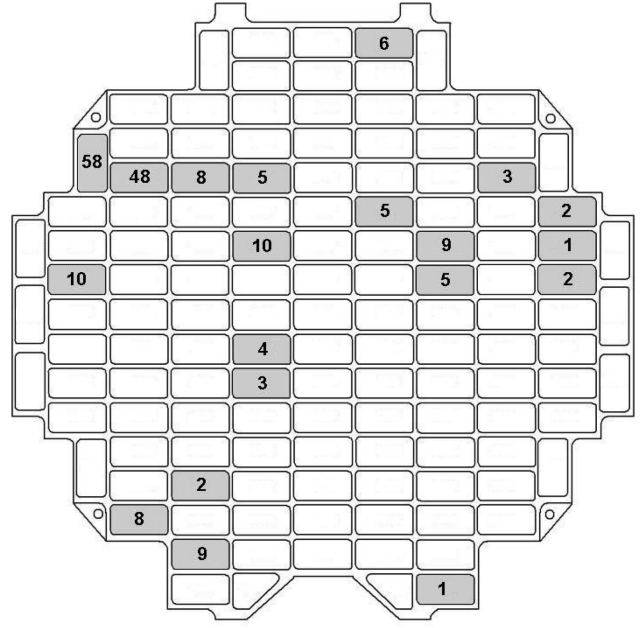


Fig. 22. Spatial distribution of tracks in Level 3 scan of extracted aerogel cells. Extracted cells are shown shaded; the number in those cells is the observed number of tracks. Note that the large numbers of tracks in cells 12 and 23 are predominantly very short tracks.

The crater data are shown in Fig. 23 (the fit is the solid line). Above a particle diameter of  $10 \mu\text{m}$ , the aerogel track and foil crater data overlap substantially. However, below this size there is a divergence that increases as particle size decreases.

In Hörz et al. (2006), the aerogel data that was used agrees at large particle sizes with that presented here, but differs below  $10 \mu\text{m}$ . In the Level 3 scan data here, all the extracted blocks have been used to obtain the cumulative size distribution. However, in Hörz et al. (2006), only two blocks were used, namely blocks C012 and C023. As can be seen from Fig. 22, these are the only two blocks with large numbers of tracks and the latter were dominated by small tracks and hence small particles. As was shown in Hörz et al. (2006) (and reproduced here on Fig. 23) the flux based on just these blocks is fully compatible with that from the foil crater data down to particle sizes of 1 or  $2 \mu\text{m}$ . Below this, the aerogel data rolls off, indicating the limits of resolution have been reached. The reason why the track data from aerogel blocks C012 and C023 differs from that given by the Level 3 analysis based here on more blocks, is that the former appear to contain a cluster of impacts that has occurred on a spatial scale of centimeters across the collector; this is the only such cluster in the larger sample. Given that this cluster is dominated by small particles, the cumulative size distribution is accordingly influenced at small sizes in the two analyses by the relative areas considered. As described in detail by Westphal et al. (2008), this clustering is poorly understood at present.

Table 6. Fits to cumulative size distribution, of the form  $y = ax^b$ , with  $x$  in  $\mu\text{m}$ .

Data set	Impactor size range ( $\mu\text{m}$ )	$a$	$b$
Aerogel Level 2, Equation 13	10–2000	47,100	$-1.22 \pm 0.06$
Aerogel Level 3, Equation 21	1–100	11,900	$-0.76 \pm 0.01$
Aerogel (all), Equation 22	1–200	14,100	$-0.86 \pm 0.01$
Foil craters, Equation 23; Hörz et al. 2006	0.05–100	125,800	$-1.72 \pm 0.05$
DFMI, Tuzzolino et al. 2004; Equation 24	1–200	1,622,000	$-2.55 \pm 0.15$
DFMI (excluding small sizes and including large sizes), Equation 25	5–600	182,000	$-1.74 \pm 0.05$

The results obtained during the post-flight analysis from the aerogel and foils can be compared to those obtained during the cometary encounter by the real-time DFMI (Tuzzolino et al. 2003). The data obtained by DFMI during the encounter were analyzed in Tuzzolino et al. (2004) and in more detail in Green et al. 2004. Two points emerged. First, the slope of the cumulative size distribution varied as the spacecraft passed closer to the comet (within 3700 km, referred to as the inner coma) and then travelled further away (outer coma). Second, above particle sizes of approximately 100  $\mu\text{m}$ , an excess of particles was reported, which was not included in any fits. For comparison to the data here, the DFMI data were converted from particle mass ( $m$ ) to particle size ( $r$ ) (with density 2400  $\text{kg m}^{-3}$ ) and are shown plotted on Fig. 23 along with all the other data sets. A fit to the DFMI data from  $1 < r < 100 \mu\text{m}$  yielded:

$$\text{Cumulative size distribution per m}^2 = 1622000 D_p^{-2.55 \pm 0.15} \quad (24)$$

(with regression coefficient  $-0.9785$ ). As expected, the power  $-2.55$  is equal to the power of the equivalent mass distribution ( $-0.85$ ) reported by Tuzzolino et al. (2004) and Green et al. (2004). In Fig. 23 above 10  $\mu\text{m}$  in particle size, DFMI, craters, and aerogel tracks all yield similar results. The discrepancies between the data sets only emerge significantly at smaller particle sizes, with extreme divergence between DFMI and the other data sets showing up at 1  $\mu\text{m}$ . In the DFMI data, the results for the smallest size particles were obtained from the most sensitive impact detector which had a surface area of 20  $\text{cm}^2$ .

When comparing the size distribution measured during encounter and those measured after the return, the large difference in the power of the cumulative size distributions (Table 6) can be seen to lie in two effects. First, the fits in the foil and aerogel analyses include data for impactors greater than order 100  $\mu\text{m}$  in size. In the fits to the DFMI encounter data (Tuzzolino et al. 2004; Green et al. 2004), this part of the size distribution was excluded as it was considered to be due

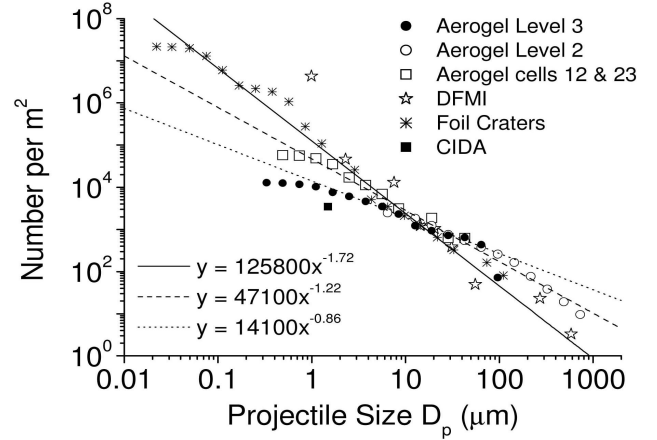


Fig. 23. Cumulative particle size distribution based from all data sets: aerogel Levels 2 and 3 scans (data presented herein), aerogel cells 12 and 23 (Hörz et al. 2006), craters in foils (Hörz et al. 2006), and the DFMI (Tuzzolino et al. 2004). The parameterizations of the fit curves shown are given in Table 6.

to an excess of large grains (similar to that reported by the Giotto encounter with comet Halley, e.g., McDonnell et al. [1991] and also partly as it was of low statistical significance at 7 impacts). If the data at large sizes ( $r > 100 \mu\text{m}$ ) were included, the data point at the smallest sizes is then not compatible with the fit of a single power law. Accordingly, if we remove the data point at the smallest size but include those at the largest sizes, we obtain:

$$\text{Cumulative size distribution per m}^2 = 182000 D_p^{-1.74 \pm 0.15} \quad (25)$$

(with regression coefficient of  $-0.9787$ ). There are thus two equally statistically valid fits (Equations 24 and 25), but with different slopes, depending on which end of the size range is excluded. Based on comparison with the other data here, it is the DFMI datum at smallest sizes that appears anomalous, as even allowing for clustering events, the other detectors do not reproduce such a high flux at small sizes and the DFMI data at this size are spread over a time period incompatible with a single cluster impact. In Green et al. (2004), the DFMI data were divided into time windows (corresponding to different stages of the encounter with the comet). The power of the size distribution was found to vary greatly depending on the time interval chosen, ranging from  $-0.9$  to  $-2.25$  near closest encounter, rising to  $-3.39$  some 600+ s after the encounter, when a burst of counts was detected. It should also be noted that the other active instrument during encounter, Cometary and Interstellar Dust Analyzer (CIDA; with a very small active area) was designed to produce time-of-flight mass spectra from impacts of small particles (size  $> 0.1 \mu\text{m}$ ), and it observed a flux significantly smaller than that predicted by the other methods extrapolated to such scales (Kissel et al. 2004); the single cumulative datum at approximately 1  $\mu\text{m}$  projectile size of CIDA (see Fig. 23) falls below most of the post-flight crater and track analysis by approximately a factor of 2–10.

Taken together, the various DFMI, foil, and aerogel data sets indicate that there was significant temporal variation in the particle flux and size distribution during encounter (DFMI) and that there were significant inhomogeneities in the spatial distribution of the cumulative particle flux measured upon sample return (foil craters and aerogel tracks), particularly at smaller sizes, e.g., 1  $\mu\text{m}$  scale and below. Obtaining a single flux or cumulative size distribution is thus difficult, as it depends on the time period considered, the particle size range used, and/or the location on the spacecraft of the detector. However, an appropriate cumulative size distribution can be obtained if a set of constraints is applied:

1. Use the combined flux from the encounter and ignore any temporal variations.
2. Include the particle size range up to largest sizes (mm scale), i.e., do not treat large grains as an excess. The various data sets here that satisfy these constraints produce a cumulative size distribution that is compatible across all the individual data sets for sizes  $>10 \mu\text{m}$  and is best described by Equation 13.
3. For sizes below 10  $\mu\text{m}$ , discrete clusters of particles are observed and how many are included in the data set and normalized to what collecting area can greatly influence the reported cumulative size distribution.

The range of slopes shown in Fig. 23 at small sizes reflects variation in these parameters acting differently in the various data sets. The three fits shown in Fig. 23 illustrate this. A small number of clusters (potentially one) normalized to a large collection area yields a distribution with a shallow slope (Equation 22). Data with a few clusters and a moderate area yields an intermediate slope (which is well-represented by the extrapolation of Equation 13 to smaller sizes), while use of several clusters in a normalizing area restricted to the cluster regions increases the slope to that of Equation 23 or greater (e.g., Equation 24). However, it should be noted that at the smallest sizes measured by DFMI, the flux was not compatible with the other measurements, either in absolute number or in the time distribution of the signals (which are incompatible with coincident hits inside a cluster).

These results can be compared to the cumulative size distributions from previous cometary encounters. The power of the size distribution from 1P/Halley was given as approximately  $-3.0$  (McDonnell et al. 1991) or  $-(2.6 \pm 0.2)$  (Fulle et al. 2000), although this was found to depend on both particle size and distance from the nucleus. By contrast, the dust-grain size distribution measured during encounter at 26P/Grigg-Skjellerup had a slope of  $-0.93$  (McDonnell et al. 1993). Ground-based observations of cometary dust mass distributions have also been made. For example, based on observations of comet Hale-Bopp combined with modelling and simulations, it is predicted that the small particle distribution in the size range 0.1 to 20  $\mu\text{m}$  had a size-distribution slope of  $-3$  (Levasseur-Regourd et al. 2007). The time-resolved Stardust data suggest considerable spatial and

temporal variation in the size distribution of freshly liberated dust from a single comet, while the cumulative Wild 2 observations seem to suggest differences from comet to comet.

## CONCLUSIONS

The Stardust mission successfully returned cometary dust grains captured in aerogel after being freshly emitted from comet 81P/Wild 2. Analysis of the tracks in the aerogel has permitted an estimate of the total cometary particle flux intercepted by the dust collector. The tracks in the aerogel divide into several categories depending on the variable composition and structure of the particles. There are solid grains that remain mostly intact during capture, and more friable grains with either a less cohesive structure or a substantial volatile content. The latter may also contain smaller grains of well-consolidated materials.

Laboratory impacts into aerogel have provided calibrations that were used to obtain Stardust cometary particle cumulative size distributions and provided samples as references for composition analysis teams. Study of 15% of the aerogel yielded 177 well-identified tracks over 50  $\mu\text{m}$  in length, which, extrapolated to the whole cometary tray, suggests that some 1180 tracks of this length or above are contained in the aerogel blocks. This is a rich harvest of cometary materials awaiting detailed analysis.

The cumulative size distribution and flux obtained for Wild 2 shows non-uniform features in both short time and spatial regimes. For particle sizes greater than 10  $\mu\text{m}$  all the measurement methods used by Stardust produced similar results. However, at smaller sizes, measurement of the particle size (or mass) distribution by different methods produced significantly different results that are not readily explained at this time; they may relate to the differing detection thresholds of the diverse methods or to spatial and temporal heterogeneities of the coma dust at the scale of individual detector surfaces, e.g., stream effects in the coma and localized point sources (some of which may be close to the spacecraft, i.e., break-up of larger particles after emission from the comet nucleus, as discussed by Westphal et al. 2008).

*Acknowledgments*—We thank NASA for supporting the Preliminary Examination period for the Stardust mission from project funds as well as through the Stardust Participating Scientist Program. The able support of the curatorial staff, including J. Warren, R. Bastien, and K. Messenger at the Johnson Space Center is gratefully acknowledged. Constructive reviews by T. J. Ahrens and J.-C. Liou were greatly appreciated. PPARC provided support for participation by groups in the United Kingdom. The Natural History Museum provided additional funds to assist in analysis.



Editorial Handling—Dr. Christian Koeberl

## REFERENCES

- Anderson W. W. and Ahrens T. J. 1994. Physics of interplanetary dust capture via impact into organic polymer foams. *Journal of Geophysical Research* 99:2063–2071.
- Brownlee D. E., Tsou P., Anderson J. D., Hanner M. S., Newburn R. L., Sekanina Z., Clark B. C., Hörz F., Zolensky M. E., Kissel J., McDonnell J. A. M., Sandford S. A., and Tuzzolino A. J. 2003. Stardust: Comet and interstellar dust sample return mission. *Journal of Geophysical Research* 108, doi:10.1029/2003JE002087.
- Brownlee D. E., Hörz F., Newburn R. L., Zolensky M., Duxbury T. C., Sandford S., Sekanina Z., Tsou P., Hanner M. S., Clark B. C., Green S. F., and Kissel J. 2004. Surface of young Jupiter family comet 81P/Wild 2: View from the Stardust spacecraft. *Science* 304:1764–1769.
- Brownlee D., Tsou P., Aléon J., Alexander C. M. O'D., Araki T., Bajt S., Baratta G. A., Bastien R., Bland P., Bleuet P., Borg J., Bradley J. P., Brearley A., Brenker F., Brennan S., Bridges J. C., Browning N., Brucato J. R., Brucato H., Bullock E., Burchell M. J., Busemann H., Butterworth A., Chaussidon M., Chevront A., Chi M., Cintala M. J., Clark B. C., Clemett S. J., Cody G., Colangeli L., Cooper G., Cordier P. G., Daghljan, C., Dai Z., D'Hendecourt L., Djouadi Z., Dominguez G., Duxbury T., Dworkin J. P., Ebel D., Economou T. E., Faurey S. A. J., Fallon S., Ferrini G., Ferroir T., Fleckenstein H., Floss C., Flynn G., Franchi I. A., Fries M., Gainsforth Z., Gallien J.-P., Genge M., Gilles M. K., Gillet P., Gilmour J., Glavin D. P., Gounelle M., Grady M. M., Graham G. A., Grant P. G., Green S. F., Grossemy F., Grossman L., Grossman J., Guan Y., Hagiya K., Harvey R., Heck P., Herzog G. F., Hoppe P., Hörz F., Huth J., Hutcheon I. D., Ishii H., Ito M., Jacob D., Jacobsen C., Jacobsen S., Joswiak D., Kearsley A. T., Keller L., Khodja H., Kilcoyne A. L. D., Kissel J., Krot A., Langenhorst F., Lanzirrotti A., Le L., Leshin L., Leitner J., Lemelle L., Leroux H., Liu M.-C., Luening K., Lyon I., MacPherson G., Marcus M. A., Marhas K., Matrajt G., Meibom A., Mennella V., Messenger K., Mikouchi T., Mostefaoui S., Nakamura T., Nakano T., Newville M., Nittler L. R., Ohnishi I., Ohsumi K., Okudaira K., Papanastassiou D. A., Palma R., Palumbo M. O., Pepin R. E., Perkins D., Perronnet M., Pianetta P., Rao W., Rietmeijer F., Robert F., Rost D., Rotundi A., Ryan R., Sandford S. A., Schwandt C. S., See, T. H., Schlutter D., Sheffield-Parker J. A., Simonovici S., Sitnitsky S. I., Snead C. J., Spencer M. K., Stadermann F. J., Steele A., Stephan T., Stroud R., Susini J., Sutton S. R., Taheri M., Taylor S., Teslich N., Tomeoka K., Tomioka N., Toppani A., Trigo-Rodríguez J. M., Troadec D., Tsuchiyama A., Tuzzolino A. J., Tylliszczak T., Uesugi K., Velbel M., Vellenga J., Vicenzi E., Vincze L., Warren J., Weber I., Weisberg M., Westphal A. J., Wirick S., Wooden D., Wopenka B., Wozniakiewicz P. A., Wright I., Yabuta H., Yano H., Young E. D., Zare R. N., Zega T., Ziegler K., Zimmerman L., Zinner E., and Zolensky M. 2006. Comet Wild 2 under a microscope. *Science* 314:1711–1716.
- Burchell M. J., Cole M. J., McDonnell J. A. M., and Zarnecki J. C. 1999a. Hypervelocity impact studies using the 2 MV Van de Graaff accelerator and two-stage light-gas gun of the University of Kent at Canterbury. *Measurement Science Technology* 10:41–50.
- Burchell M. J., Thomson R., and Yano H. 1999b. Capture of hypervelocity particles in aerogel: In ground laboratory and low Earth orbit. *Planetary and Space Science* 47:189–204.
- Burchell M. J., Graham G., and Kearsley A. 2006. Cosmic dust collection in aerogel. *Annual Reviews of Earth and Planetary Science* 34:385–418.
- Domínguez G., Westphal A. J., Jones S. M., and Phillips M. L. F. 2004. Energy loss and impact cratering in aerogels: Theory and experiment. *Icarus* 172:613–624.
- Fulle M., Lvasseur-Regourd A. C., McBride N., and Hadamcik N. 2000. In situ dust measurements from within the coma of 1P/Halley: First-order approximation with a dynamical dust model. *The Astronomical Journal* 119:1968–1977.
- Green S. F., McDonnell J. A. M., McBride N., Colwell M. T. S. H., Tuzzolino A. J., Economou T. E., Tsou P., Clark B. C., and Brownlee D. E. 2004. The dust mass distribution of comet 81P/Wild 2. *Journal of Geophysical Research* 109:1–12.
- Hörz F., Cintala M., Bernhard R. P., and See T. H. 1994. Dimensionally scaled penetration experiments—Aluminum targets and glass projectiles 50  $\mu\text{m}$  to 3.2 mm in diameter. *International Journal of Impact Engineering* 15:257–280.
- Hörz F., Cintala M. J., Zolensky M. E., Bernhard R. B., Davidson W. E., Haynes G., See T. H., Tsou P., and Brownlee D. E. 1998. Capture of hypervelocity particles with low-density aerogel. NASA TM-98-201792. 58 p.
- Hörz F., Zolensky M. E., Bernard R. P., See T. H., and Warren J. L. 2000. Impact features and projectile residues in aerogel exposed on Mir. *Icarus* 147:559–579.
- Hörz F., Bastien R., Borg J., Bradley J. P., Bridges J. C., Brownlee D. E., Burchell M. J., Cintala M. J., Dai Z. R., Djouadi Z., Dominguez G., Economou T. E., Faurey S. A. J., Floss C., Franchi I. A., Graham G. A., Green S. F., Heck H., Hoppe P., Huth J., Ishii H., Kearsley A. T., Kissel J., Leitner J., Leroux H., Marhas M., Messenger K., Schwandt C. S., See T. H., Snead S., Stadermann F. J., Stephan T., Stroud R., Teslich N., Trigo-Rodríguez J. M., Tuzzolino A. J., Troadec D., Tsou P., Warren J., Westphal A., Wozniakiewicz P. J., Wright I., and Zinner E. 2006. Impact features on Stardust: Implications for comet 81P/Wild 2 dust. *Science* 314:1716–1719.
- Kearsley A. T., Burchell M. J., Hörz F., Cole M. J., and Schwandt C. S. 2006. Laboratory simulations of impacts upon aluminum foils of the Stardust spacecraft: Calibration of dust particle size from comet Wild 2. *Meteoritics & Planetary Science* 41:167–180.
- Kearsley A. T., Graham G. A., Burchell M. J., Cole M. J., Dai Z., Teslich N., Chater R. J., Wozniakiewicz, Spratt J., and Jones G. 2007. Analytical scanning and transmission electron microscopy of laboratory impacts on Stardust aluminum foils: Interpreting impact crater morphology and the composition of impact residues. *Meteoritics & Planetary Science* 42:191–210.
- Kissel J., Krueger F. R., Silén J., and Clark B. C. 2004. The cometary and interstellar dust analyzer at comet 81P/Wild 2. *Science* 304:1774–1776.
- Kistler S. S. 1931. Coherent expanded aerogels and jellies. *Nature* 127:741.
- Kitazawa Y., Fujiwara A., Kadono T., Imagawa K., Okada Y., and Uematsu K. 1999. Hypervelocity impact experiments on aerogel dust collector. *Journal of Geophysical Research* 104:22,035–22,052.
- Levasseur-Regourd A. C., Mukai T., Lasue J., and Okada Y. 2007. Physical properties of cometary and interplanetary dust. *Planetary and Space Science* 55:1010–1020.
- McDonnell J. A. M., Lamy P. L., and Pankiewicz G. S. 1991. In *Comets in the post-Halley era*, vol. 2, edited by Newburn R. L., Neugebauer M., and Rahe J. Norwell, Massachusetts: Kluwer Academic. pp. 1043–1073.

- McDonnell J. A. M., McBride N., Beard R., Bussoletti E., Colangeli L., Eberhardt P., Firth J. G., Grard R., Green S. F., and Greenberg J. M. 1993. Dust particle impacts during the Giotto encounter with comet Grigg-Skjellerup. *Nature* 362:732–734.
- Tsou P., Brownlee D. E., Lurance M. R., Hrubesh L., and Albee A. L. 1988. Intact capture of hypervelocity micrometeoroid analogs. 19th Lunar and Planetary Science Conference. pp. 1205–1206.
- Tsou P., Brownlee D. E., Sandford S. A., Hörz F., and Zolensky M. E. 2003. Wild 2 and interstellar sample collection and Earth return. *Journal of Geophysical Research* 108:1–21.
- Tsou P., Brownlee D. E., Anderson J. D., Bhaskaran S., Chevront A. R., Clark B. C., Duxbury T., Economou T., Green S. F., Hanner M. S., Hörz F., Kissel J., McDonnell J. A. M., Newburn R. L., Ryan R. E., Sandford S. A., Sekanina Z., Tuzzolino A. J., Vellinga J. M., and Zolensky M. E. 2004. Stardust encounters comet 81P/Wild 2. *Journal of Geophysical Research* 109:1–8.
- Tuzzolino A. J., Economou T. E., McKibbin R. B., Simpson J. A., McDonnell J. A. M., Burchell M. J., Vaughan B. A. M., Tsou P., Hanner M. S., Clark B. C., and Brownlee D. E. 2003. Dust Flux Monitor Instrument for the Stardust mission to comet Wild 2. *Journal of Geophysical Research* 108:1–24.
- Tuzzolino A. J., Economou T. E., Clark B. C., Tsou P., Brownlee D. E., Green S. F., McDonnell J. A. M., McBride N., and Colwell M. T. S. H. 2004. Dust measurements in the coma of comet 81P/Wild 2 by the Dust Flux Monitor Instrument. *Science* 304:1776–1780.
- Westphal A. J., Bastien R. K., Borg J., Bridges J., Brownlee D. E., Burchell M. J., Cheng A. F., Clark B. C., Djouadi Z., Floss C., Franchi I., Gainsforth Z., Graham G., Green S. F., Heck P. R., Hor'anyi M., Hoppe P., Hörz F., Huth J., Kearsley A., Leroux H., Marhas K., Nakamura-Messenger K., Sandford S. A., See T. H., Stadermann F., Tsitrin S., Tsou P., Warren J. L., Wozniakiewicz P. J., and Zolensky M. E. 2008. Discovery of non-random spatial distribution of impacts in the Stardust cometary collector. *Meteoritics and Planetary Science* 43. This issue.
-